

K_s NUMBER COUNTS IN THE GROTH AND COPPI FIELDS¹

DAVID CRISTÓBAL-HORNILLOS,² MARC BALCELLS,² MERCEDES PRIETO,² RAFAEL GUZMÁN,³ JESÚS GALLEGÓ,⁴
 NICOLÁS CARDIEL,⁴ ÁNGEL SERRANO,⁴ AND ROSER PELLÓ⁵

Received 2002 December 12; accepted 2003 May 30

ABSTRACT

We have used William Herschel Telescope/INGRID K_s images on two high-latitude fields, the Coppi and Groth strips, to obtain galaxy number counts over ~ 180 arcmin², to a depth of $K_s \sim 21.0$. Detection efficiency corrections as a function of object size have been calculated on each pointing. We have used a signal-to-noise threshold in two complementary half-exposure images to remove spurious detections. Our data cover the range from $K_s = 14.5$ to $K_s = 21.0$, so they are useful for investigating a previously reported change in the number count slope ($d \log N/dm$) at $K \sim 17$. We find a slope $\gamma_b = 0.54\text{--}0.63$ for $K < 17.5$ and a slope $\gamma_f = 0.25\text{--}0.29$ for $K > 17.5$. A total contribution from galaxies to the extragalactic background light (EBL) in the K band of $\nu I_\nu = 10.5$ nW m⁻² sr⁻¹ has been calculated. This K -band EBL coming from galaxies accounts for only $\sim 50\%$ of the recent measurements of the diffuse EBL. Standard number count models fail to reproduce the observed slope change at $K \sim 17.5$ unless elliptical and spiral formation is pushed to $z \lesssim 2$.

Subject headings: cosmology: observations — galaxies: evolution — galaxies: high-redshift — galaxies: photometry — surveys

1. INTRODUCTION

Near-infrared (NIR) galaxy number counts offer a number of advantages over optical counts for testing galaxy evolution models. The NIR light of galaxies is roughly constant across wavelength, implying that K -corrections are small and reasonably easy to model. The NIR light is less affected than optical light by recent bursts of star formation, and hence galaxies are selected by something closer to their mass than in optical surveys; the latter map the rest-frame ultraviolet (UV) emission of galaxies at high redshift, and hence are biased toward actively star-forming galaxies of any mass. Finally, lower dust extinction at longer wavelengths restricts the use of dust as a wild card when a given model fails to match the data.

NIR surveys, however, have traditionally suffered from poor number statistics, specifically a low area \times depth product, as a result of the small format of NIR detectors in comparison to optical CCDs. To date, K -band surveys mosaicking over a wide area reach depths of $K \sim 19.5$ (Glazebrook et al. 1994; Gardner et al. 1996; Huang et al. 1997; McCracken et al. 2000; Väisänen et al. 2000; Huang et al. 2001; Martini 2001), while deeper surveys cover a few square arcminutes (Gardner, Cowie, & Wainscoat 1993; Cowie et al. 1994; Djorgovski et al. 1995; McLeod et al. 1995; Moustakas et al. 1997; Bershadsky, Lowenthal, & Koo 1998; Totani et al. 2001b).

NIR number counts are particularly useful in determining the cosmological model when combined with redshift

distributions, optical number counts, and high-resolution images from the *Hubble Space Telescope* (HST), the latter providing galaxy sizes, surface brightness profiles, and axis ratios.

Counts at optical wavelengths may be fitted by a power law in the range $18 < B < 27$ with slope ~ 0.46 (Tyson 1988; Lilly, Cowie, & Gardner 1991) and present an excess by factors of 3–4 at $B \sim 24$ over no-evolution models (Tyson 1988; Maddox et al. 1990; Lilly et al. 1991; Metcalfe et al. 1991). However, for K -band number counts a change in the slope ($d \log N/dm$) around $16 < K < 18$ has been reported, and the overall number counts may be fitted by two power laws. Gardner et al. (1993) find a bright slope, $\gamma_b = 0.67$, in the range $10 < K < 16$, and a faint slope, $\gamma_f = 0.26$, at $18 < K < 23$. However, other authors (Bershadsky et al. 1998; McCracken et al. 2000) find a steeper faint slope, $\gamma_f = 0.36$. Different solutions have been adopted to match the optical and NIR number count models to the data: luminosity function evolution, either in density (ϕ^*) or in luminosity (M^*) (Lilly et al. 1991); merger evolution (Glazebrook et al. 1994); or introduction of a new population of faint blue dwarf galaxies at intermediate redshifts $z \sim 0.4$ (Babul & Rees 1992). A faint slope lower than $\gamma = 0.4$ implies that the total contribution from galaxies to the total extragalactic background light (EBL) has an upper limit, while slopes $\gamma > 0.4$ lead to an Olbers' paradox problem, i.e., a divergence of the total light contributed by faint sources.

In the context of a wider study of galaxy evolution, we are carrying out a deep optical-NIR survey that plans to increase the depth \times area product by a notable factor. The COSMOS Survey is described in § 2. In this paper we present K_s number counts in two COSMOS fields, the Groth strip and the Coppi field, that confirm the change in the slope of the number counts at $K \sim 17.5$. We describe the fields in § 2, the observations in § 3, and the reduction strategy in § 4. We then go on to describe source extraction and estimates of detection efficiency and reliability in § 5 and the procedure to separate stars and galaxies in § 6. In § 7 we present the number counts and a comparison to number count models.

¹ Based on observations made with the William Herschel Telescope, operated on the island of La Palma by the Isaac Newton Group of Telescopes in the Spanish Observatorio del Roque de los Muchachos of the Instituto de Astrofísica de Canarias.

² Instituto de Astrofísica de Canarias, C/ Vía Láctea, 38200 La Laguna, Canary Islands, Spain.

³ Department of Astronomy, 477 Bryant Space Center, University of Florida, Gainesville, FL.

⁴ Departamento de Astrofísica, Universidad Complutense de Madrid, 28040 Madrid, Spain.

⁵ Laboratoire d'Astrophysique de l'Observatoire Midi-Pyrénées, 14 Avenue Edouard-Belin, F-31400 Toulouse, France.

Throughout the paper we use a cosmology with $H_0 = 70$ km s⁻¹ Mpc⁻¹, $\Omega_M = 0.3$, and $\Omega_\Lambda = 0.7$.

2. THE COSMOS SURVEY

The COSMOS survey will be defined elsewhere; here only a brief summary is given. We aim to cover ~ 0.5 square degrees of sky in the *K* band and in complementary bands *U*, *B*, *V*, *R*, *I*, and *J*. The survey should therefore provide *K*-band magnitudes ($\sim R$ -band rest frame) for $2 < z < 3.5$ luminous blue compact galaxies (LBCGs) (Phillips et al. 1997; Guzmán et al. 1997, 1998), Lyman break galaxies (LBGs) (Steidel et al. 1996; 1999; Lowenthal et al. 1997), as well as for galaxies without strong star formation activity. Lowenthal et al. (1997) estimate a surface density of over 10^4 LBGs deg⁻², and hence the survey should provide more than a thousand sources for detailed *K*-band spectroscopic follow-up with the upcoming generation of NIR multiobject spectrographs, e.g., FLAMINGOS (Elston 1998) and EMIR (Balcells 1998; Manescau et al. 2002).

The COSMOS survey depth and area coverage makes it useful also for the definition of homogeneous, large samples of galaxies at $0.5 < z < 1$. In this redshift domain, galaxy morphology, surface brightness and color distributions, and axial ratios are available from *HST* imaging (Roche et al. 1996; Marleau & Simard 1998; Aguerri & Trujillo 2002). The *K*-band data provide *J* or *H* rest-frame magnitudes, key data for constraining stellar mass content of these galaxies.

This paper presents galaxy number counts for two of the COSMOS survey fields, the Groth strip and the Coppi field. The Groth-Westphal strip (Groth et al. 1994) has been the subject of numerous studies by several groups. The field comprises 28 WFPC2 pointings, of total area 113 arcmin², defining a linear strip on the sky at position angle P.A. = 40°3'48" centered on R.A. = 14^h16^m38^s.8, decl. = 52°16'52" (J2000), at Galactic latitude $b = +60^\circ$. Of these, 27 pointings are exposed for 4400 s in F814W and for 2800 s in F606W (the “4.4 ks” fields) and a single WFPC2 field has a total exposure of 25.2 ks in F814W and F606W (see Ratnatunga et al. 1995). The *HST* 4.4 ks images provide number counts to roughly $I \sim 25$ (Roche et al. 1996). Morphology and photometry are provided within the Medium Deep Survey (MDS) database (Ratnatunga, Griffiths, & Ostrander 1999).

The Coppi field covers a $10' \times 10'$ area centered on R.A. = H^h59^m31^s.0, decl. = 29°14'43" (J2000). The field contains the gamma-ray blazar 1156+295 and has been observed by ACIS-I on board the *Chandra X-Ray Observatory* for 75 ks by Coppi et al. (2000), as well as in *B* and *R*, to a depth of $B = R = 26$ (Coppi & Guzmán 2001).

3. OBSERVATIONS

Observations were carried out with the near-infrared camera INGRID on the Cassegrain focus of the William Herschel Telescope (WHT) during two runs of three nights each in 2000 April 10–12 and 2001 June 28–30. In a related campaign, we have mapped the Groth strip flanking fields with the 3.5 m telescope in the Calar Alto Spanish-German Astronomical Center (CAHA) (A. Serrano et al. 2003, in preparation).

INGRID images the WHT focal plane on a 1024×1024 HgCdTe Rockwell array. Main parameters of the camera are given in Table 1. In the 2000 run, the camera used a tem-

TABLE 1
ISAAC NEWTON GROUP RED IMAGING DEVICE
MAIN PARAMETERS

Parameter	Value
Gain ^c (e ⁻ ADU ⁻¹).....	3.9–4.1
Readout noise (e ⁻) ^c	16–25
Full-well capacity (ADU) ^c	$\sim 28,000$ – $30,000$
Pixel size (μm) ^c	18.5
Pixel scale (arcsec pixel ⁻¹) ^c	0.25, ^a 0.238 ^b
Field of view.....	4'16", ^a 4'04" ^b
Size of detector (arcmin) ^c	1024×1024
Bad pixels ^c	$\sim 2\%$
Linearity (at 10,000 ADU).....	$\sim 2\%$
Wavelength range (μm) ^c	0.8–2.5
Quantum efficiency ^c	$\sim 58\%$ at $J(1.2 \mu\text{m})$, $\sim 58\%$ at $H(1.65 \mu\text{m})$, $\sim 62\%$ at $K(2.2 \mu\text{m})$
Full-frame readout time (s) ^c	0.76

^a With the temporary collimator (before 2001 March 22).

^b With the new foreoptics (after 2001 March 22).

^c Source: <http://www.ing.iac.es/Astronomy/instruments/ingrid/index.html>.

porary collimator, which was replaced by the definitive lens in 2001 March. As a result, both the plate scale and the throughput varied between the two runs. Atmospheric conditions were photometric, with seeing ranging from 0".6 to 0".75 FWHM in 2000 April and photometric with seeing of 0".60–1".30 FWHM in 2001 June. Integration times were chosen to keep the count levels in the images well within the linear regime of the detector (see § 4). Individual images were six co-adds of 10.296 s each, and the total combined exposure was 90 minutes in Groth and 2 hr in Coppi during the 2000 run. In 2001, in order to obtain similar count levels with the higher throughput of INGRID, individual images were eight co-adds of 8.264 s, again with a total combined exposure time of 90 minutes in the Groth's pointings. The typical background in K_s was 11.9 mag arcsec⁻² in 2000 April run and 11.7 mag arcsec⁻² in 2001 June run. Dither patterns were tailored to the geometry of each field. In the Coppi field we did three pointings. For each, a nine-point dither pattern was used, with 15" offsets in the north and east directions. In the Groth strip the chip was rotated to a sky position angle of 40°06' for optimal coverage of the strip imaged with *HST*, and we did six pointings of $4'.27 \times 4'.27$ each in 2000 April and five pointings of $4'.06 \times 4'.06$ each in 2001 June. In the Groth strip a dither pattern of eight pointings was used with an offset 20" in the direction of the strip and 7" in the perpendicular direction. The separation between frames was $4'.27$ and $4'.06$ in the first and second runs, respectively. In both fields, adjacent dither sequences overlap to produce a uniform exposure time map in the final mosaicked image, except in the mosaic outer edges. The center coordinates of each of the 11 Groth pointings and three Coppi pointings are given in Table 2.

Standard stars (Persson et al. 1998) were observed during each night at different air masses in order to correct each individual image from atmospheric extinction and to obtain the photometric zero point for each night. We estimated photometric zero-point uncertainties to be less than 0.03 mag in 2000 April and less than 0.05 mag in 2001 June. Photometric coefficients are given in Table 3. Flat-field images were obtained both from light-on and light-off dome flats

TABLE 2
CENTER COORDINATES, FINAL POINT-SPREAD FUNCTION FWHM, AND 50% DETECTION EFFICIENCIES FOR POINT SOURCES IN THE
THREE POINTINGS IN COPPI AND THE 11 POINTINGS IN GROTH

Pointing (1)	R.A. (J2000.0) (2)	Decl. (J2000.0) (3)	Exposure (s) (4)	FWHM (arcsec) (5)	50% Efficiency (mag) (6)	r_e div (arcsec) (7)	F (8)	Detection Threshold (9)
Coppi1	11 59 40.17	29 17 17.98	7522	0.75	21.03	0.5, 0.8	3.0	0.9
Coppi2	11 59 21.83	29 17 17.99	7167	0.69	21.03	0.5, 0.8	3.0	0.9
Coppi3	11 59 21.83	29 12 07.97	7584	0.67	21.03	0.5, 0.8	3.0	0.9
Groth01	14 15 08.20	52 00 39.04	5728	0.60	20.88	0.5, 0.8	3.0	0.9
Groth02	14 15 26.23	52 03 53.72	5737	0.61	20.88	0.5, 0.8	3.0	0.9
Groth03	14 15 44.30	52 07 08.31	5736	0.64	20.88	0.5, 0.8	3.0	0.9
Groth04	14 16 02.42	52 10 22.98	5618	0.72	20.85	0.55, 0.85	3.0	0.9
Groth05	14 16 20.58	52 13 37.61	5740	0.74	20.85	0.55, 0.85	3.0	0.9
Groth06	14 16 38.79	52 16 52.32	7166	0.89	20.87	0.65, 0.95	4.0	0.7
Groth07	14 16 52.75	52 19 30.81	5793	0.87	20.68	0.65, 0.95	3.0	0.9
Groth08	14 17 08.86	52 22 27.22	4939	1.27	20.21	0.9, 1.2	4.0	0.7
Groth09	14 17 25.01	52 25 23.45	6409	0.73	20.86	0.5, 0.8	3.0	0.9
Groth10	14 17 41.19	52 28 19.55	5726	0.61	21.24	0.5, 0.8	3.0	0.9
Groth11	14 17 57.40	52 31 15.52	5662	0.94	20.28	0.7, 1.0	4.0	0.7

NOTE.—Units of right ascension are hours, minutes, and seconds, and units of declination are degrees, arcminutes, and arcseconds. Col. (7) shows the r_e for group division to define “point sources,” “intermediate-size objects,” and “large objects” (see § 5). Col. (8) is the identification for the Gaussian filter applied by SExtractor. Col. (9) is the detect threshold relative to the background rms (DETECT_THRESH in SExtractor).

and from source-free sky exposures when the sky brightness was rising near the twilight. Subtraction of two flat-field exposures with equal exposure time and different illumination level provides a flat-field image that maps the pixel-to-pixel sensitivity variations of the detector, free from thermal component of the dome, telescope, and optics. Series of dark-frame images of all the exposure times used in each night were also taken.

When the first run of observations took place, the linearity of the detector was not well determined, so we did our own linearity test. To do so, the telescope was pointed to an illuminated part of the dome and series of exposures with integration times 1, 2, 3, 4, 6, 8, 10, 12, 14, 16, 18, 20, 22, and 24 s were taken. Deviations from linearity are approximately 2% up to $\sim 10,000$ ADU. INGRID shows a small memory effect; the bias level is slightly higher after a saturated or near-saturated exposure. We interspersed each linearity exposure with 1 and 2 s exposures and ended the entire series with 10 exposures of 1 s. These additional measurements indicated that the memory effect disappears after a single low-count readout, that the dome lamp had sufficient brightness stability, and that INGRID exposures of the order of 1–2 s are stable and photometrically reliable.

TABLE 3
PHOTOMETRIC CALIBRATION COEFFICIENTS

Date	Zero Point ^a	Extinction ^b	rms ^c
2000 Apr 20	22.51	0.10	0.02
2000 Apr 21	22.50	0.10	0.03
2000 Apr 22	22.47	0.09	0.02
2001 Jun 28	22.89	0.11	0.03
2001 Jun 29	22.70	0.05	0.04
2001 Jun 30	22.80	0.10	0.03

^a Magnitude per 1 ADU s⁻¹.

^b Extinction coefficient (mag air mass⁻¹).

^c The rms of standard star photometric solution.

4. REDUCTION

The reduction of the data sets followed standard steps. First, individual images were corrected from nonlinearity. To compute the linearity correction function, the median levels of the linearity exposures were plotted against exposure time. The linear part of the response curve (up to ~ 5000 ADU) was fitted with a straight line to establish the run of counts with time expected under linear conditions. A second-order polynomial fitted to the ratio linear/measured versus measured counts gave the linearity correction function to apply to the data. The linearity correction function is shown in Figure 1. Linearity corrections remain below 8%

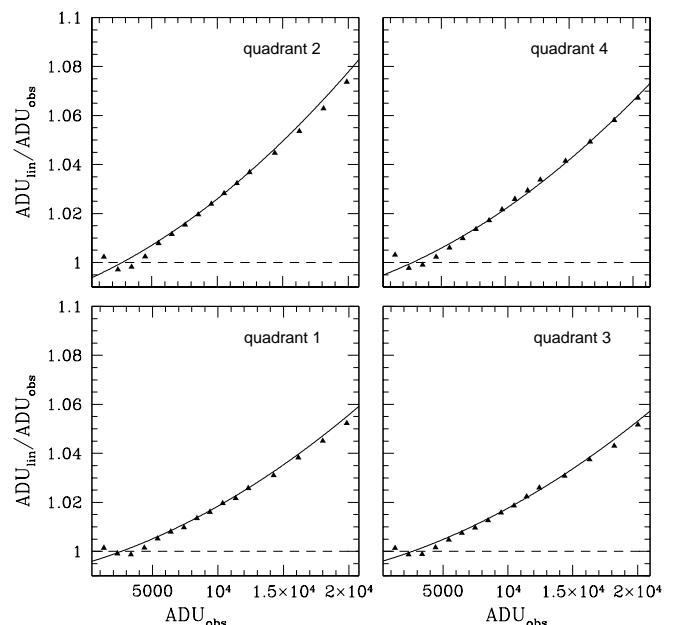


FIG. 1.—Linearity correction for 2001 run. Each panel corresponds to a quadrant of the detector. A second-order polynomial was fitted to ADU_{lin}/ADU_{obs} vs. ADU_{obs} .

up to 20,000 ADU. Since the count level in science frames was kept always below 11,000 ADU, we can be confident that our data are free from noticeable nonlinearity effects.

All the images were dark current-subtracted using a dark-averaged image with the same exposure time. Flat-field calibration images were constructed for each night by subtracting low-illumination flats from high-illumination flats (see § 3). The subtraction removes the thermal component coming from the warm optics, telescope structure, and dome from the flat-field image, so that the flat-field image maps the pixel-to-pixel sensitivity variations in the detector. This flat-field image is used to flatten all the individual images. The thermal component is removed at the sky-subtraction phase. Sky subtraction, bad-pixel and cosmic-ray removal, and final combination of the sky-subtracted individual images were done using DIMSUM package within IRAF (Stanford, Eisenhardt, & Dickinson 1995). In a first pass, a sky image is made for each individual image using the median of eight neighboring images. Then a threshold algorithm is applied to the ratio between image and a median filtered image to find cosmic rays in each individual image. A bad-pixel mask is provided to make bad and hot pixel correction; this mask is updated by considering pixels with multiple cosmic-ray detections in several images. Finally, the sky-subtracted images are combined to obtain a preliminary image that is used to create two mask images, one extended-object mask to cover most of the objects in the field and another bright-core mask to restore pixels in the cores of bright sources that might have been mistaken as cosmic rays. In a second pass (mask pass) those masks are used to obtain a more accurate sky image for each individual image, which is used for sky subtraction. Finally, the individual images are corrected from atmospheric extinction and combined to obtain a final image of the field. An exposure time map is also obtained. The nonflatness of the final images is less than 6×10^{-5} of the sky (peak to peak in the uniformly exposed area).

5. PHOTOMETRY

To extract the sources from the images SExtractor (Bertin & Arnouts 1996) has been used. Source detection in SExtractor is governed by three main parameters: detection kernel, minimum area, and detection threshold. The first two are well constrained as a function of the seeing in each image. To constrain the last one, DETECT_THRESH, an agreement between a good detection efficiency and a low number of spurious detections at the faintest magnitudes is necessary. The filter applied to each field before extraction and the detection thresholds are given in Table 2.

To determine the detection efficiency, the brightest sources in the images were taken as models that were scaled in flux and reintroduced into the science images. Three different bins in half-light radius r_e , determined from SExtractor circular apertures, namely, “point sources,” “intermediate-size objects,” and “large objects,” were considered in order to estimate detection efficiencies as a function of source size. The three group division depends on the FWHM in the image. Point sources are defined as those whose r_e is lower or equal than the r_e of the stars; this value plus $0''.3$ is used to separate the intermediate and large classes (these values appear in col. [7] in Table 2). Injected sources were placed far enough from the real ones to avoid source confusion and any problems with SExtractor deblending algorithm. Then

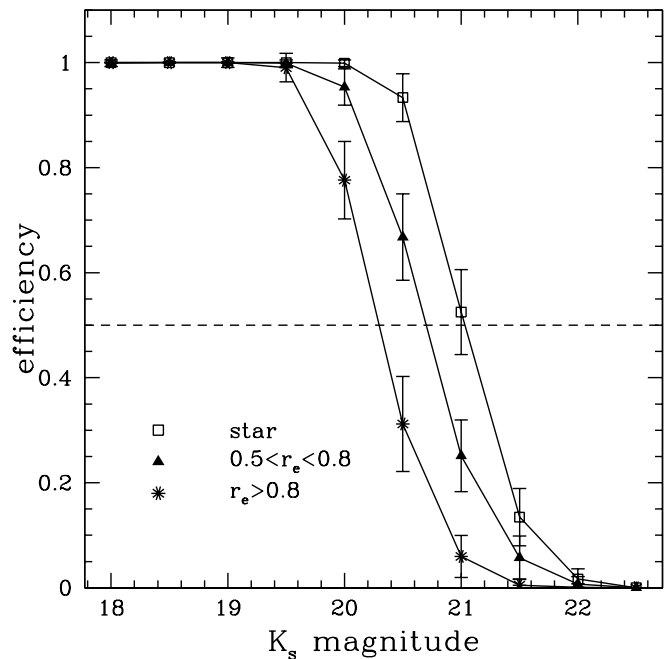


Fig. 2.—Detection efficiency function for Coppi field for three galaxy apparent size groups, “point sources” ($r_e \leq 0''.5$), “intermediate size objects” ($0''.5 < r_e \leq 0''.8$), and “large objects” ($r_e > 0''.8$).

SExtractor was used to recover the objects, and detection efficiency was recorded as a function of magnitude for each size group. Figure 2 shows the detection efficiency functions for the three size groups considered in our Coppi fields. Efficiency drops abruptly near the detection limit, and it is a strong function of image size: the 50% detection level is ~ 0.75 mag deeper for point sources than for large objects. The behavior of the efficiency function is identical to that found by Bershadsky et al. (1998). Detection efficiency has been measured and corrected separately for each observed pointing, as it varies with the seeing and with the throughput of INGRID. The limiting magnitude, given as the 50% detection depth for point sources, is given in Table 2 for each survey pointing. For the pointings in Coppi, with roughly equal exposure time and seeing, the same detection efficiency functions are used, the same was done for the first three pointings in Groth and for Groth04 and Groth05.

In order to quantify the effects of source confusion in our detection efficiency estimates, trial simulations have been run in which injected sources are not required to fall far away from real sources in the field. From these experiments, we estimate that source confusion may lower our detection efficiencies by less than 3% over almost the entire magnitude range and by $\sim 10\%$ near the 50% detection level of each object class. The detection efficiencies listed in Tables 5, 6, and 7 therefore might be slightly overestimated ($\sim 1 \sigma$) near the detection limit. However, we use those values throughout the paper since confusion corrections are difficult to apply to the data.

To determine detection reliability from science images requires adopting a method to discriminate between real faint sources and those produced by noise. We have implemented a procedure, inspired by that used by Bershadsky et al. (1998), that uses images with half-exposure time constructed from two exclusive halves of the data. Spurious sources should be produced by a noise peak in an individual image

of the many (~ 100) that are co-added for each field, and hence each noise peak should appear in one of the two half-time images only. With this assumption, at the positions of all the sources detected by SExtractor in the total-time image we perform photometry on the two half-time images, with the same adaptable apertures (double-image mode in SExtractor). All sources with signal-to-noise ratio (S/N) below a given limit S/N_{lim} in any one of the two half-time images are considered spurious. The value of S/N_{lim} is chosen by examining the histograms of flux differences between the half-exposure images for candidate spurious detections (see Fig. 3). A good discrimination of spurious sources leads to a bimodal histogram of magnitude differences, while too high an S/N_{lim} leads to the inclusion of real

sources and to a magnitude-difference histogram with a single peak centered on $m_1 - m_2 = 0$. From the histograms built for a range of S/N_{lim} the value $S/N_{\text{lim}} = 2.2$ for the half-time images was considered the best, and this value is used to separate spurious sources from real ones in our images. The spurious-to-total detection ratio and the reliability function (1 minus the spurious fraction) are shown in Figure 4. As also found by Bershadsky et al. (1998), the reliability function is 100% over most of the magnitude range and drops abruptly to zero near the 50% efficiency magnitude. We found that spurious sources were more abundant on the lower exposure edges of the mosaics. To avoid a complicated spurious source correction that varies over the frames, the reliability analysis is constrained to the portion

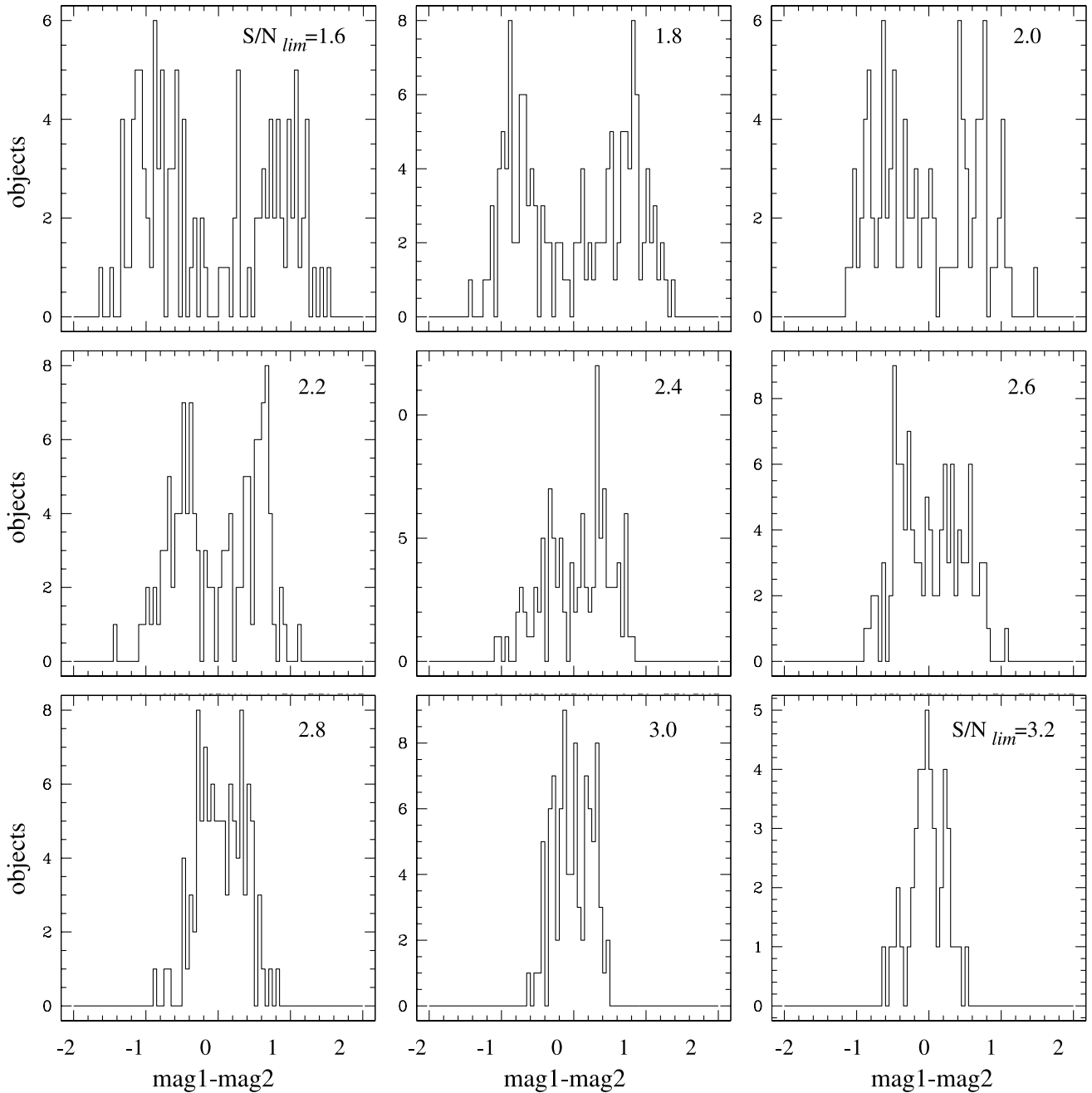


FIG. 3.—Histogram of magnitude differences between the half-exposure images for candidate spurious detection with different S/N_{lim} values: 1.6, 1.8, 2.0, 2.2, 2.4, 2.6, 2.8, 3.0, and 3.2. Each histogram is built with candidate spurious sources at the given S/N_{lim} that are not deemed spurious for a cutoff value of ($S/N_{\text{lim}} - 0.2$).

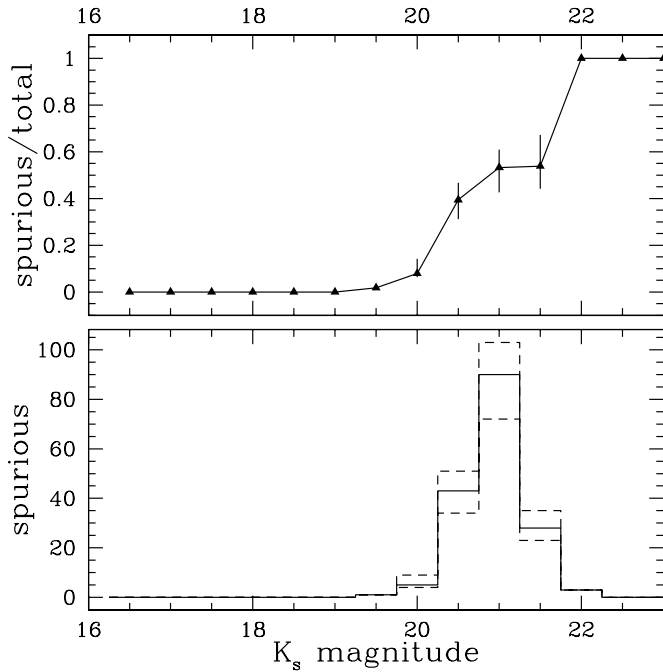


FIG. 4.—*Top*: Fraction of spurious sources vs. magnitude for the Coppel field. Error bars correspond to the fraction of spurious sources obtained with $S/N_{\text{lim}} = 2.2 \pm 0.2$. *Bottom*: Number of spurious sources vs. magnitude for the same field. Dashed-line histograms represent the number of spurious sources obtained using $S/N_{\text{lim}} = 2.2 \pm 0.2$.

of the frames with maximum, uniform exposure time. Source extraction is also constrained to these maximum exposure portions of the frames.

Although our method of spurious source detection is based on a S/N criterion on the final image (taking as real sources those with $S/N > 2.2$ in both half-time images, and hence, roughly $S/N > 3.1$ on the total-time image), a few of the sources identified as spurious by this method have high S/N in the total-time image (up to $S/N > 5$). Considering Gaussian statistics, the probability of a source with $S/N > 5$ having $S/N < 2.2$ in one of the two half-time images is less than 0.009. In our data a 13.7% of the sources with $S/N > 5$ are removed considered as spurious.

In order to assess the determination of the detection efficiency and reliability on our images, we have calculated both corrections on a set of synthetic images using *artdata.mkobject* in IRAF. Synthetic frames were generated with the same Gaussian sky noise as science frames, and simulated galaxy images span the same range of magnitudes and r_e as observed galaxies. We obtained the detection efficiencies and the number of spurious detections by comparing the pixel positions where objects had been injected to the position of the objects identified by SExtractor. We obtain a 50% detection depth for point sources ~ 0.3 mag fainter than that determined using real sources. The spurious fraction is significantly lower than that coming from our half-time images. We suspect that these discrepancies arise from the fact that synthetic galaxy images are smoother and geometrically simpler than real galaxies and that the Gaussian noise fails to reproduce the true sky noise. Together, the efficiency and reliability determinations based on synthetic data lead to an overestimate of the depth of the data and an underestimate of the spurious sources, which lead to an artificial rise in the counts at the faint limit of the survey.

6. STAR-GALAXY SEPARATION

Doing a good star-galaxy separation is important especially at bright magnitudes. At fainter magnitudes the number of stars in high galactic latitude fields is almost negligible in comparison with the number of galaxies. To separate galaxies and star counts, we first used the star-galaxy separation procedure in SExtractor with the default configuration. This separation did not work well at magnitudes between 17.5 and 19.0 in those pointings with worse seeing. This was a problem for pointings in Groth where the point-spread function was $\text{FWHM} \geq 0.9$ (Table 2).

In the Groth strip we have made use of the Groth-Westphal catalog from F606 and F814 *HST*/WFPC2 images to improve the star-galaxy separation (see Ratnatunga et al. 1999).⁶ Pointlike objects (stars and QSOs) in this catalog are used to estimate the number of stars in each of our pointings. Figure 5 shows the distinct location of stars and galaxies in a color-color diagram. $V_{606} - I_{814}$ and $I_{814} - K_s$ color were computed using “total” best SExtractor magnitude from *HST*/WFPC2 in F606 and F814 filters and WHT/INGRID K_s images. The number of stars in common between the K_s and *HST* images for each of our Groth K_s pointings is divided by the ratio between the *HST*+ K_s area and K_s area in the pointing to obtain the number of stars per magnitude bin expected in each K_s pointing. This number is then corrected using the “point sources” efficiency correction (§ 5) and subtracted from the object counts. At bright magnitudes, $K_s < 16.5$, because of small statistic to obtain star counts in K_s area from stars in *HST*+ K_s area, we have used SExtractor star-galaxy separation parameter ($\text{CLASS_STAR} < 0.8$) to remove stars in Groth strip point-

⁶ See also <http://archive.stsci.edu/mds>.

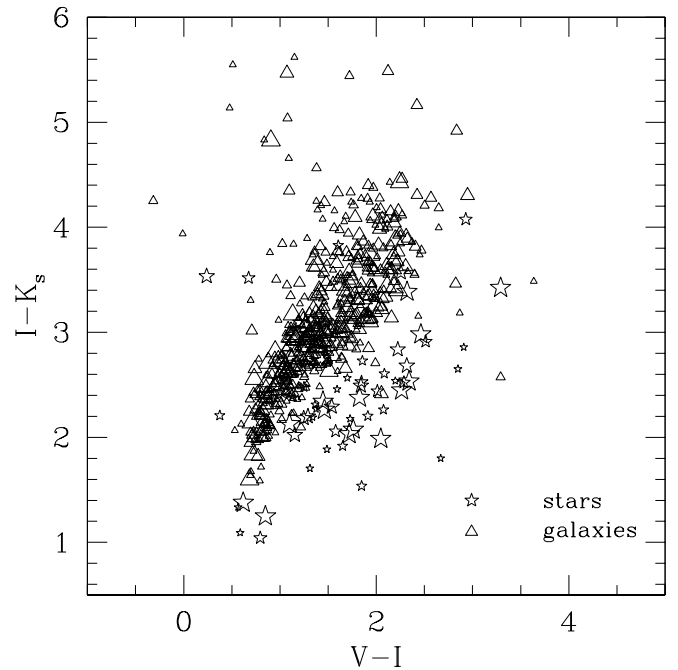


FIG. 5.— $V_{606} - I_{814}$ vs. $I_{814} - K_s$ colors in Groth strip fields. Triangles represent galaxies, and stars represent sources classified as stellar in the MDS Groth catalog. The range in sizes represent different K_s magnitude bins for $K_s \leq 17.25$, $17.25 < K_s \leq 17.75$, $17.75 < K_s \leq 18.25$, $18.25 < K_s \leq 18.75$, and $18.75 < K_s \leq 19.25$. Larger symbols correspond to brighter magnitudes.

ings. Despite some Groth pointings have a higher seeing, in the common HST and K_s area both methods give the same result for $K_s < 16.5$ objects. In Figure 6 the star counts in Groth corrected from detection efficiency are compared with counts models from Spagna (2001). The solid line is the prediction for Galactic coordinates $b = 60^\circ, l = 180^\circ$, and the dashed line corresponds to $b = 60^\circ, l = 90^\circ$ closer to

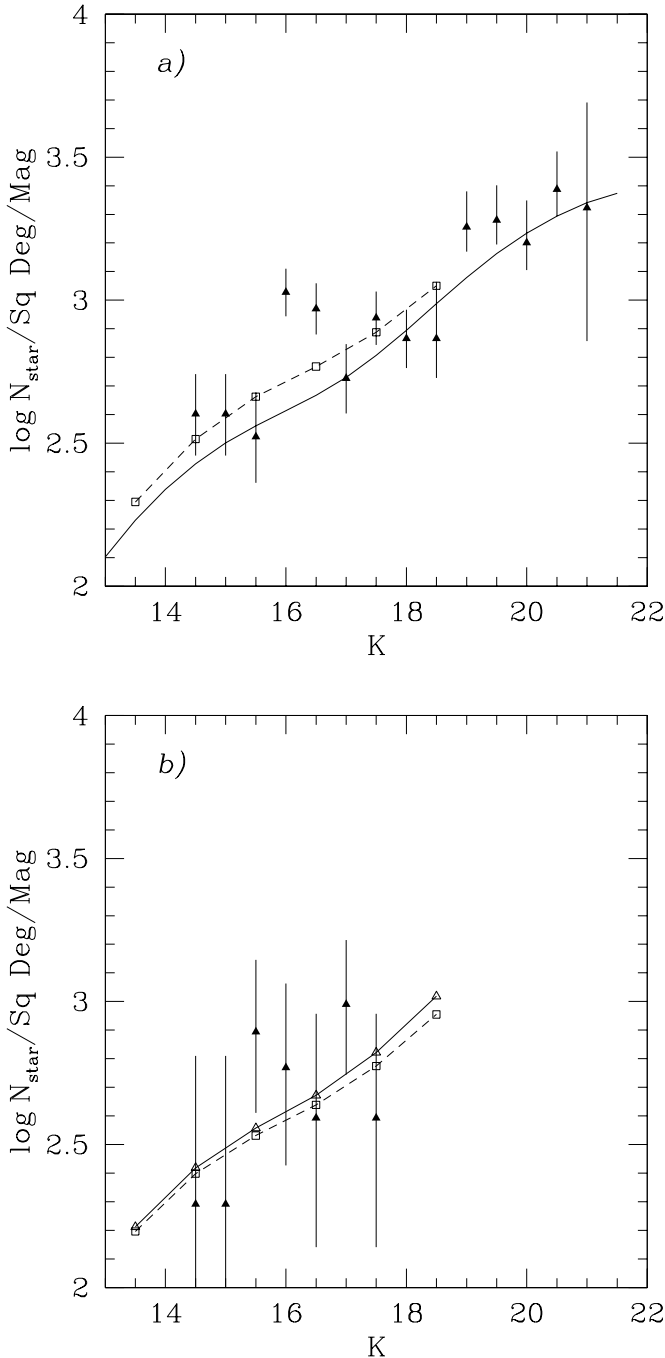


FIG. 6.—(a) Star counts in Groth derived using HST F814W images, corrected from detection efficiency (filled triangles). The solid line is the prediction for Galactic coordinates $b = 60^\circ, l = 180^\circ$, and the open squares and the dashed line correspond to $b = 60^\circ, l = 90^\circ$ (Spagna 2001), close to Groth strip ($b = 60^\circ, l = 95^\circ$). Error bars correspond to counting statistics (Gehrels 1986) added in quadrature to uncertainties in efficiency correction determination. (b) Star count prediction for Coppi field ($b = 78^\circ 57', l = 45^\circ 31'$) models are for Galactic coordinates $b = 80^\circ, l = 0^\circ$ (solid line) and $b = 80^\circ, l = 90^\circ$ (dashed line).

Groth strip ($b = 60^\circ 22', l = 95^\circ 38'$). Table 4 presents the star number counts in the Groth strip.

In the Coppi field we have tried to do the star-galaxy separation using optical and near-infrared colors as in Väisänen et al. (2000). B and R images from WIYN (Wisconsin-Indiana-Yale-NOAO) 3.5 m telescope in KPNO (Coppi et al. 2000) have been used to derive $B-R$ and $R-K_s$ colors, using SExtractor BEST magnitude, for the K_s -detected objects. For magnitudes brighter than $K_s = 17.75$ the fraction of K_s sources matched in B and R frames is 96.0%, whereas in the $K_s = 19$ bin the number of sources with B and R counterparts is 64.1%. The galaxy-star separation done by SExtractor ($\text{CLASS_STAR} < 0.8$) and by colors were compared, showing a good agreement (Fig. 7). The separation between galaxies and stars by colors is quite good, with some overlap at the red end; it would be possible to do a good statistical star-galaxy separation with these sets of colors in a wider area than our K_s area in Coppi. Because of the small area and the good seeing in Coppi (FWHM ~ 0.7), we finally have decided to use the SExtractor stellarity index at magnitudes brighter than $K_s = 19.25$ and not to do the star-galaxy separation in the faintest magnitude bins where star count contribution to the total counts is small and the star identification is more complicated because of the seeing and the small size of galaxies.

Table 4 shows the contribution of stars to galaxy counts in different magnitude bins computed for the Groth strip field. The correction in $\log N$ due to stars is lower than 0.05 at magnitudes fainter than 19.5 (using the numbers for star counts in Groth strip, similar to that for Coppi; Fig. 6). By not applying star correction to the three Coppi fields, the error introduced in the number counts for the 14 pointings is lower than 0.01 dex. This justifies our not applying a star-galaxy separation correction in the Coppi field.

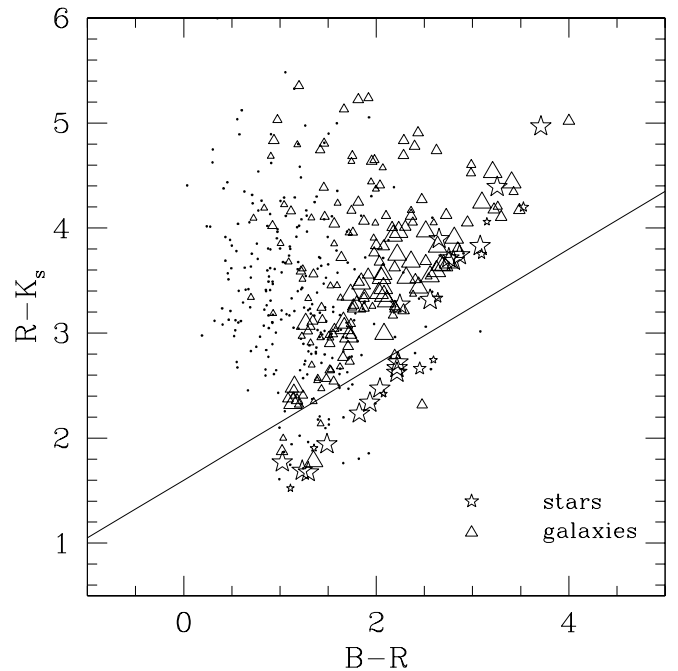


FIG. 7.— $B-R$ vs. $R-K_s$ colors in Coppi fields. Symbols are as in Fig. 5, defined by the stellarity index from SExtractor. Dots are objects with $K_s > 19.25$. The line is the one used by Väisänen et al. (2000) for doing the star-galaxy separation.

TABLE 4
CORRECTION DUE TO STAR COUNTS: GROTH STRIP

K_s (1)	N_g (2)	N_s (3)	$\log N_s$ (4)	σ_l (5)	σ_u (6)	rms_l (7)	rms_u (8)	N_s/N_g (9)	$\log(1 + N_s/N_g)$ (10)	A_s (11)
14.5	50.3	400.2	2.602	0.145	0.140	0.370	0.197	7.96	0.95	0.02998
15.0	452.6	400.2	2.602	0.145	0.140	0.313	0.180	0.88	0.28	0.02998
15.5	452.6	333.5	2.523	0.161	0.155	0.251	0.158	0.74	0.24	0.02998
16.0	754.4	1,067.0	3.028	0.084	0.083	0.154	0.113	1.41	0.38	0.02998
16.5	1,911.0	933.9	2.970	0.090	0.089	0.139	0.105	0.49	0.17	0.02998
17.0	3,320.0	533.7	2.727	0.123	0.120	0.195	0.134	0.16	0.06	0.02998
17.5	6,308.0	867.2	2.938	0.094	0.093	0.088	0.073	0.14	0.06	0.02998
18.0	8,290.0	733.9	2.866	0.103	0.101	0.203	0.138	0.09	0.04	0.02998
18.5	11,950.0	733.8	2.866	0.138	0.199	0.184	0.129	0.06	0.03	0.02998
19.0	14,620.0	1,803.0	3.256	0.086	0.125	0.099	0.081	0.12	0.05	0.02998
19.5	17,170.0	1,905.0	3.280	0.085	0.122	0.102	0.082	0.11	0.05	0.02998
20.0	27,700.0	1,589.0	3.201	0.096	0.148	0.066	0.058	0.06	0.02	0.02998
20.5	46,610.0	2,442.0	3.388	0.094	0.133	0.090	0.074	0.05	0.02	0.02444
21.0	69,130.0	2,105.0	3.323	0.466	0.368	0.03	0.01	0.00278

NOTE.—Cols. (2) and (3) are the galaxy and star counts in units of $N \text{ mag}^{-1} \text{ deg}^{-2}$; cols. (5), (6), (7), and (8) are 84.13% confidence upper and lower limits and the 1σ uncertainty in the determination of the mean between pointings; col. (10) is the correction to $\log N$ if stars were not removed from galaxy counts; col. (11) is the area where star counts were calculated. The area where galaxy counts were calculated is given in Table 5.

7. RESULTS AND DISCUSSION

Differential galaxy counts (number $\text{mag}^{-1} \text{ deg}^{-2}$) are presented in Figure 8a and Tables 5 (Coppi), 6 (Groth), and 7 (total). The counts have been extracted from the deepest, equal-S/N regions of the both fields (144 arcmin^2 in Groth and 37 arcmin^2 in Coppi, $\sim 60\%$ of our surveyed area). There is an excellent agreement between the counts in both fields; the differences are due to counting statistics and efficiency correction uncertainties. Only in $K_s = 19.5$ is there a significant difference in the counts between both fields, Coppi showing a 3σ excess. Below $K = 18$, differences are due to low raw counts in the smaller Coppi field.

Counts are corrected down to 50% detection efficiency in each pointing and for each size group, as described in § 5. For point sources, the 50% limit corresponds to 21.03 mag

for the deepest field in Coppi, 20.88 mag for 2000 April Groth strip data, and 20.21 mag for the shallowest of the 2001 June Groth data. Sources have roughly $S/N > 3$ within the seeing area at these limiting magnitudes. Detection efficiency corrections are calculated and applied in each source group and in each individual pointing. The resulting effective completeness correction for each magnitude bin, defined as

$$\text{effective completeness correction} = \frac{2 \times \text{raw counts/area}}{\text{corrected counts}}, \quad (1)$$

is given in column (4) of Tables 5, 6 and 7.

We provide two independent estimates of the galaxy number count errors. The first is a proper error calculation

TABLE 5
 K_s DIFFERENTIAL NUMBER COUNTS IN GROTH STRIP

K_s (1)	Raw (2)	N (3)	Effective Completeness Correction (4)	N_{low} (5)	N_{up} (6)	$\log N$ (7)	σ_l (8)	σ_u (9)	rms_l (10)	rms_u (11)	A (12)
14.5	1.0	50.3	1.00	8.6	167.1	1.702	0.766	0.521	1.702	0.306	0.03977
15.0	9.0	452.6	1.00	304.8	659.9	2.656	0.172	0.164	0.143	0.107	0.03977
15.5	9.0	452.6	1.00	304.8	659.9	2.656	0.172	0.164	0.110	0.088	0.03977
16.0	15.0	754.4	1.00	562.0	1004.3	2.878	0.128	0.124	0.113	0.089	0.03977
16.5	38.0	1,911.0	1.00	1,602.5	2,274.4	3.281	0.076	0.076	0.088	0.073	0.03977
17.0	66.0	3,320.0	1.00	2,912.5	3,781.2	3.521	0.057	0.056	0.040	0.037	0.03977
17.5	125.4	6,308.0	1.00	5,745.6	6,923.2	3.800	0.041	0.040	0.065	0.057	0.03977
18.0	164.4	8,290.0	1.00	7,645.0	8,987.5	3.919	0.035	0.035	0.046	0.042	0.03977
18.5	236.6	11,950.0	1.00	11,137.5	13,147.0	4.077	0.031	0.041	0.029	0.027	0.03977
19.0	285.3	14,620.0	0.98	13,656.7	16,007.0	4.165	0.030	0.039	0.026	0.025	0.03977
19.5	327.6	17,170.0	0.96	16,123.0	18,634.0	4.235	0.027	0.036	0.029	0.027	0.03977
20.0	445.3	27,700.0	0.81	26,108.0	29,725.0	4.442	0.026	0.031	0.049	0.044	0.03977
20.5	521.5	46,610.0	0.68	44,046.0	49,629.0	4.668	0.025	0.027	0.026	0.025	0.03268
21.0	81.5	69,130.0	0.68	56,650.0	82,410.0	4.840	0.086	0.076	0.00345

NOTE.—Col. (2) shows the galaxy counts per interval of half-magnitude (raw counts minus star counts); col. (3) shows N is the corrected galaxy counts in units of $N \text{ mag}^{-1} \text{ deg}^{-2}$; col. (4) shows the effective completeness correction; cols. (5) and (6) show the 84.13% lower and upper limits on corrected counts; cols. (8), (9), (10), and (11) show the 84.13% confidence upper and lower limits and 1σ uncertainty in the determination of the mean between pointings; and col. (12) shows the surveyed area in deg^2 .

TABLE 6
 K_s DIFFERENTIAL NUMBER COUNTS IN COPPI FIELD

K_s (1)	Raw (2)	N (3)	Effective Completeness		N_{low} (5)	N_{up} (6)	$\log N$ (7)	σ_l (8)	σ_u (9)	rms_l (10)	rms_u (11)	\mathcal{A} (12)
			Correction (4)									
14.5.....	0.0	0.0	...		0.0	365.0	0.01022
15.0.....	2.0	391.2	1.00		139.3	911.2	2.592	0.449	0.367	2.432	0.300	0.01022
15.5.....	3.0	586.8	1.00		268.4	1161.2	2.769	0.340	0.296	0.372	0.198	0.01022
16.0.....	9.0	1,760.0	1.00		1,185.2	2,566.4	3.246	0.172	0.164	0.077	0.066	0.01022
16.5.....	8.0	1,565.0	1.00		1,024.4	2,339.2	3.194	0.184	0.175	0.124	0.096	0.01022
17.0.....	14.0	2,739.0	1.00		2,016.7	3,685.9	3.438	0.133	0.129	0.247	0.157	0.01022
17.5.....	18.0	3,521.0	1.00		2,699.6	4,564.0	3.547	0.115	0.113	0.077	0.066	0.01022
18.0.....	41.0	8,020.0	1.00		6,773.0	9,480.0	3.904	0.073	0.073	0.042	0.038	0.01022
18.5.....	62.0	12,130.0	1.00		10,621.0	14,223.0	4.084	0.058	0.069	0.079	0.067	0.01022
19.0.....	71.0	13,900.0	1.00		12,284.0	16,150.0	4.143	0.054	0.065	0.042	0.039	0.01022
19.5.....	123.0	24,340.0	0.99		22,162.0	27,166.0	4.386	0.041	0.048	0.066	0.057	0.01022
20.0.....	134.0	29,680.0	0.88		27,039.0	33,073.0	4.472	0.040	0.047	0.055	0.049	0.01022
20.5.....	154.0	46,750.0	0.64		42,122.0	52,010.0	4.670	0.045	0.046	0.075	0.064	0.01022
21.0.....	172.0	64,090.0	0.53		56,558.0	72,087.0	4.807	0.054	0.051	0.026	0.025	0.01022

NOTE.—Columns are as in Table 5.

in which errors from counting statistics at each pointing (Gehrels 1986) are added in quadrature, taking into account the estimated uncertainties in the detection efficiency corrections and the subtraction of star counts in Groth strip. This error calculation is described in detail in the Appendix. The second error estimate is a simple error of the mean, i.e., the dispersion of number counts for the 14 pointings. The two error estimates are shown as vertical bars in Figure 8b. There is a good agreement between both error estimates, except at bin $K = 17.5$, where the Groth and Coppi counts differ.

7.1. External Comparison and Counts from Complete Data

In Figure 9 we compare our combined Groth-Coppi counts to a large set of K -band number count data extracted from the literature. The latter include wide-angle, shallow surveys as well as deep, pencil-beam data, together providing number counts over a 14 mag range. We have made no distinction between K and K_s data; from our calibration

stars we find $\langle K - K_s \rangle = -0.01$, which translates into a systematic error in the number counts of less than 0.005 dex in the range $14.5 < K_s < 17.5$ and less than 0.003 dex for $K_s > 17.5$.

Our counts are in good agreement with those of the literature, both at the bright and faint ends of the distribution. However, a broad dispersion in the counts from different authors is evident in Figure 9 at all magnitudes, but especially at the bright and faint ends of the distribution. For instance, at $K = 23$, Bershadsky et al. (1998) and Moustakas et al. (1997) differ by a factor of more than 3. The reasons for this dispersion are likely to be related to incompleteness at the faint end and to the small number statistics and large-scale structure (see Huang et al. 1997 for a discussion of large-scale structure) at the bright end. Completeness corrections depend on galaxy size, surface brightness, seeing, and the detection algorithm; all of those vary among the various studies. The very definition of galaxy magnitude varies among authors. Aperture magnitudes underestimate the flux of bright sources, while isophotal magnitudes do so

TABLE 7
 COMBINED K_s DIFFERENTIAL NUMBER COUNTS IN GROTH AND COPPI

Effective Completeness											
K_s	Raw	N	Correction	N_{low}	N_{up}	$\log N$	σ_l	σ_u	rms_l	rms_u	\mathcal{A}
(1)	(2)	(3)	(4)	(5)	(6)	(7)	(8)	(9)	(10)	(11)	(12)
14.5.....	1.0	40.0	1.00	6.9	132.9	1.602	0.766	0.521	1.602	0.303	0.04999
15.0.....	11.0	440.1	1.00	309.6	617.2	2.644	0.153	0.147	0.141	0.106	0.04999
15.5.....	12.0	480.1	1.00	343.6	663.0	2.681	0.145	0.140	0.103	0.083	0.04999
16.0.....	24.0	960.2	1.00	765.7	1,199.2	2.982	0.098	0.097	0.091	0.075	0.04999
16.5.....	46.0	1,840.0	1.00	1,569.7	2,153.6	3.265	0.069	0.068	0.073	0.063	0.04999
17.0.....	80.0	3,201.0	1.00	2,844.0	3,600.6	3.505	0.051	0.051	0.046	0.042	0.04999
17.5.....	143.4	5,738.0	1.00	5,259.5	6,258.4	3.759	0.038	0.038	0.062	0.054	0.04999
18.0.....	205.4	8,235.0	1.00	7,661.5	8,850.0	3.916	0.031	0.031	0.036	0.034	0.04999
18.5.....	298.6	11,980.0	1.00	11,263.8	13,024.0	4.079	0.027	0.036	0.026	0.025	0.04999
19.0.....	356.3	14,470.0	0.99	13,635.5	15,666.0	4.160	0.026	0.034	0.022	0.021	0.04999
19.5.....	450.6	18,630.0	0.97	17,685.3	19,930.0	4.270	0.023	0.029	0.032	0.030	0.04999
20.0.....	579.3	28,100.0	0.82	26,723.0	29,854.0	4.449	0.022	0.026	0.039	0.036	0.04999
20.5.....	675.5	46,650.0	0.67	44,407.0	49,269.0	4.669	0.021	0.024	0.024	0.023	0.04291
21.0.....	253.5	65,360.0	0.57	58,908.0	72,214.0	4.815	0.045	0.043	0.020	0.019	0.01367

NOTE.—Columns are as in Table 5.

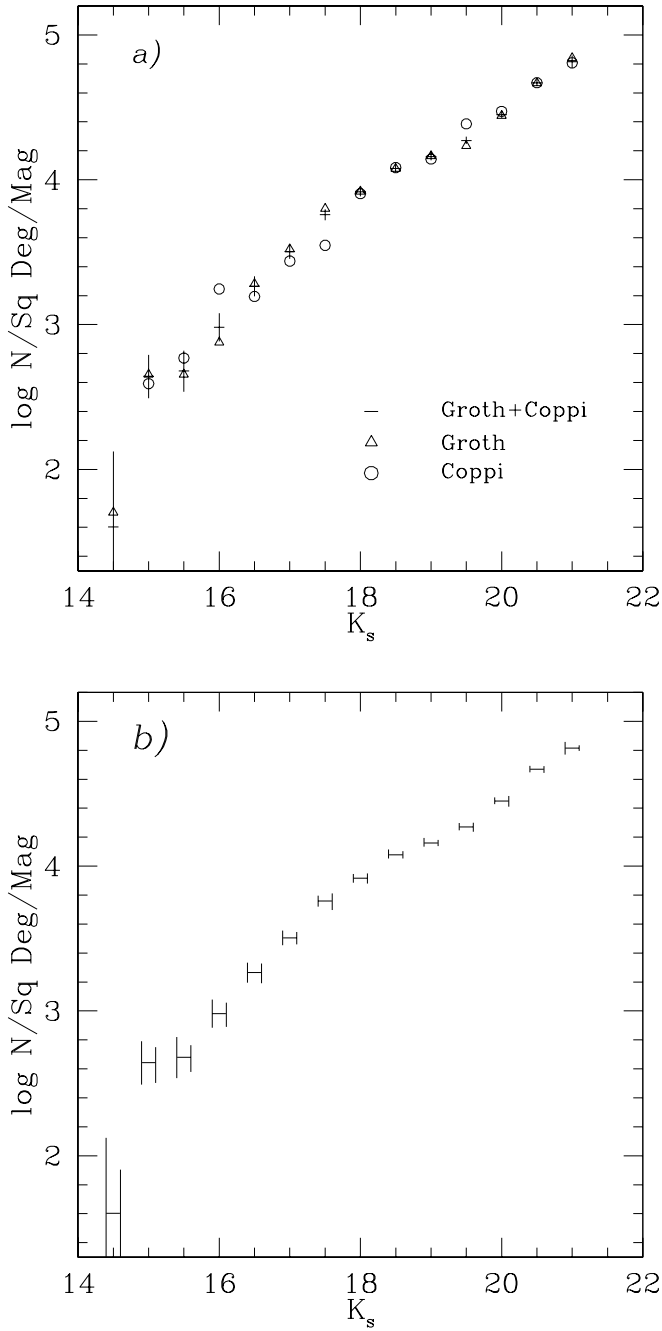


FIG. 8.—(a) Galaxy number counts in Groth and Coppi. The total counts with estimated errors are also shown. (b) Uncertainties in the Groth-Coppi combined counts are shown as vertical bars. Estimated 84.13% lower and upper limits errors are offset by -0.1 mag, while 1σ uncertainty in the determination of the mean between the different pointings are offset by 0.1 mag; the values are given in Table 7.

with faint sources. “Total” magnitudes rely on a model that generally assumes a given surface brightness profile. At intermediate magnitudes, large discrepancies may be introduced by the star-galaxy separation algorithms, which may be based on morphological classification (Glazebrook et al. 1994; Huang et al. 1997, 2001; Saracco et al. 1997, 1999; Minezaki et al. 1998; Kümmel & Wagner 2001), color-color diagrams (McLeod et al. 1995; Gardner et al. 1996; Huang et al. 1997, 2001; Väisänen et al. 2000), or Milky Way star-count models (Väisänen et al. 2000; Saracco et al. 1997),

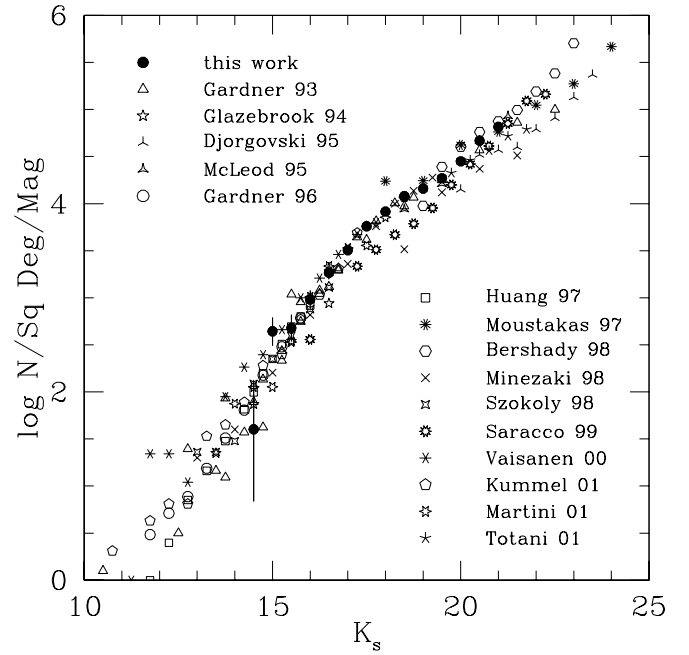


FIG. 9.—Galaxy number counts from combined Coppi and Groth data $\sim 180 \text{ arcmin}^2$. Counts from other deeper and shallower surveys are plotted for comparison.

with some works combining two methods to obtain the star counts at bright and faint magnitudes. While the observed dispersion among authors is smaller at intermediate magnitudes, this range is important to establish whether the K_s number counts change slope (see § 7.2).

To investigate the source of the dispersion, we have constructed a “complete number count distribution,” including only complete number count data, from our work and the literature. For the present purpose, we define complete data as those with more than 10 raw counts (i.e., $>3 \sigma$ measurements) and with completeness corrections lower than 5%. The first condition eliminates uncertain bright-magnitude points, while the second eliminates points near the detection limit of each survey. Published counts that are efficiency-corrected at all magnitude bins are excluded. Also excluded are counts given only in graphical form, counts where star-galaxy separation has not been performed, and counts from fields at or near obvious galaxy clusters. Our criteria for defining complete data relies on accepting each author’s criteria as to whether their data require detection efficiency corrections. Nevertheless, our approach provides a first-cut filter to take into account the largest sources of discrepancy between counts by different authors. The complete number count distribution is shown in Figure 10a.

Remarkably, the scatter among different authors is much diminished. The complete number count distribution of Figure 10a demonstrates that K -band counts derived over the years using a variety of telescopes, detectors, and source extraction algorithms are in remarkably good agreement as long as complete data are considered. This result suggests that detection efficiency correction techniques often fail to recover the true number count distribution. Our corrected counts at magnitudes $K_s \geq 20$ are above the “complete counts” of other authors by factors of 1.12, 1.37, and 1.46 at $K = 20.0$, 20.5 , and 21.0 , respectively. If the “complete counts” do reflect the true K -band galaxy number counts,

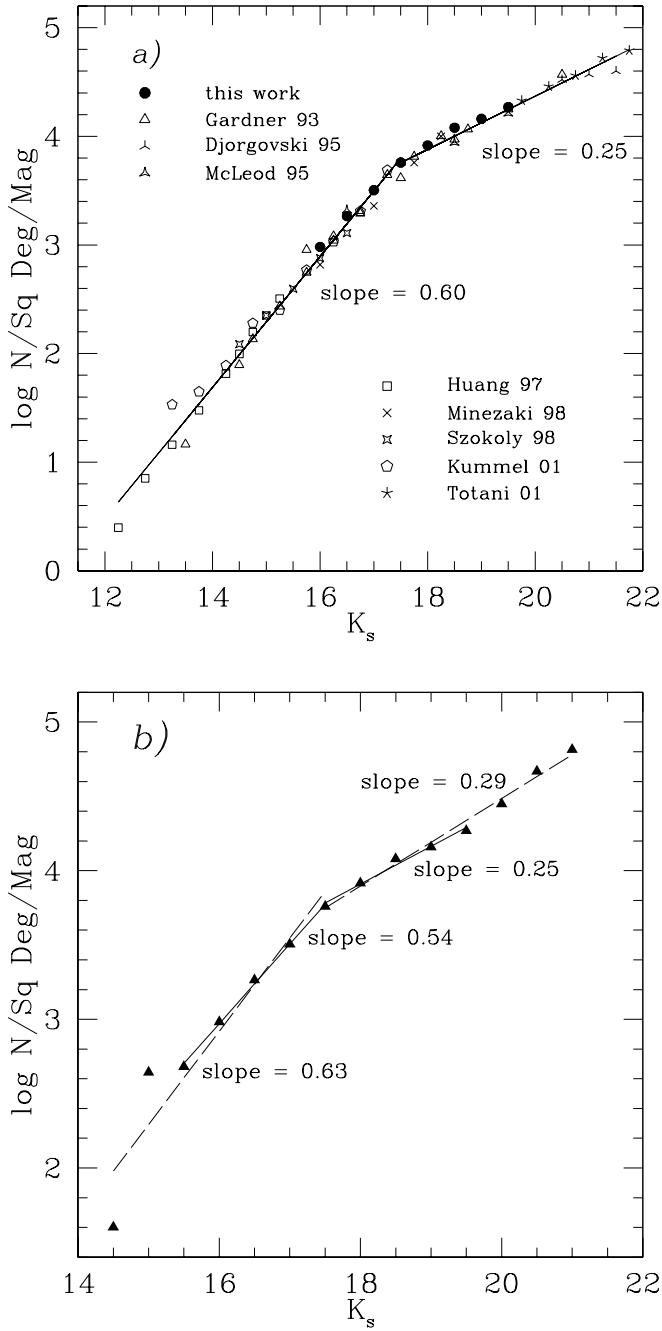


FIG. 10.—(a) Best two-power-law fit to “complete data” from our and other authors. (b) COSMOS- K_s counts fitted to two power laws using least squares (no weights), the best solution for “complete counts” (solid line) show a slope of 0.54 from $K_s = 15.5$ to $K_s = 17.5$ and a slope 0.25 from 17.5 to 19.5. The dashed line is the best two-power-law fit when all of our counts are considered.

our excess might indicate an inaccuracy in either the efficiency or the reliability corrections. The latter, involving a subjective choice of S/N_{lim} , is the main suspect. Taking a value $S/N_{\text{lim}} = 2.4$, which increases the number sources considered as spurious (see Fig. 4), our number counts would lie above “complete counts” only by factors of 1.2 at $K = 20.5$ and 21.0.

7.2. K -Band Number Count Slope

Our counts clearly show a slope change at $K_s \sim 17.5$. A similar slope change was noted by Gardner et al. (1993),

who pointed out that $B-K$ colors become progressively redder from $K = 14$ to $K = 17$, as a result of the K -correction, while at fainter than $K = 17$, median $B-K$ colors rapidly become bluer because of the blue intrinsic colors of the galaxies. Our data confirm the slope change. With our combination of depth and area, our survey covers the $15.5 < K_s < 19.5$ range with complete data and good statistics; hence it is well poised for a measurement of the slopes at the bright and faint sides of the break. Figure 10b shows the COSMOS K_s number count least-squares fit to two separate power laws (no weights). Using only complete data, the power law in the range $K_s = 15.5$ to $K_s = 17.5$ has slope $\gamma_b = 0.54$ with reduced $\chi^2 = 0.12$, while in the range $K_s = 17.5$ to $K_s = 19.5$ the slope is $\gamma_f = 0.25$ with reduced $\chi^2 = 0.95$. Figure 10b also shows that these values hardly change when all of our count data are used ($\gamma_b = 0.63$, $\chi^2/\nu = 2.91$ and $\gamma_f = 0.29$, $\chi^2/\nu = 2.53$). In Figure 10a we show the two-power-law fits to the “complete count” distribution introduced in § 7.1. For these data, the bright-end slope is $\gamma_b = 0.60$, and the faint-end slope is $\gamma_f = 0.25$. There is a good agreement between the slopes derived from our data and from the complete count distribution. In particular, the faint counts give no suggestion of an upturn down to $K_s = 21$.

Extrapolating the number counts faintward using

$$\log N(K) = a + \gamma K, \quad (2)$$

the fluxes ($\text{ergs cm}^{-2} \text{ s}^{-1} \text{ Hz}^{-1} \text{ sr}^{-1}$) contributed by galaxies fainter than a given K_0 are

$$2.19 \times 10^{-17} 10^a \frac{10^{(\gamma-0.4)K_0}}{1 - 10^{\gamma-0.4}} \quad (3)$$

if $\gamma < 0.4$.

Using the values of the slope ($\gamma_f = 0.25$) and $a = -0.65$ from the best fit to the faintest part of our complete count data (efficiency-corrected points excluded; see Fig. 10b), we derive a contribution to the EBL due to the $K \geq 22$ galaxies of $1.4 \text{ nW m}^{-2} \text{ sr}^{-1}$. The total contribution to the EBL due to galaxies has been calculated using this value and the extrapolation at bright magnitudes, from $K = 14$ up to $K = 10$, with slope $\gamma = 0.60$ derived from the “complete data” of different surveys. We have obtained $\nu I_\nu = 10.5 \text{ nW m}^{-2} \text{ sr}^{-1}$, similar to the value obtained by Totani et al. (2001a), $\nu I_\nu \leq 10.2 \text{ nW m}^{-2} \text{ sr}^{-1}$. An estimate of the uncertainty in our νI_ν may be derived by taking the steeper faint-end slope from all of our count measurements ($\gamma_f = 0.29$, $a = -1.41$; see Fig. 10b); we would then obtain $\nu I_\nu = 11.7 \text{ nW m}^{-2} \text{ sr}^{-1}$. Our measurements and those of Totani et al. (2001a), when compared with recent measurements of the diffuse EBL in the K band, i.e., $22.4 \pm 6.0 \text{ nW m}^{-2} \text{ sr}^{-1}$ (Gorjian, Wright, & Chary 2000) or $20.2 \pm 6.3 \text{ nW m}^{-2} \text{ sr}^{-1}$ (Wright 2001), show that if the faint number count slope does not change, galaxies account for only about 50% of the EBL in the K band. See Hauser & Dwek (2001) for a useful review on the cosmic infrared background measurements.

7.3. Comparison to Number Count Models

The well-defined change of slope of our K_s -band number counts is an important constraint to galaxy formation models. A full investigation is beyond the scope of this paper, but we have nevertheless inquired how well standard number count models fare when compared with our data. For

TABLE 8
GALAXY CHARACTERISTICS USED IN THE NUMBER COUNT MODEL

GALAXY TYPE (1)	SFR		Z/Z_{\odot} (4)	z_{form} (5)	DISTRIBUTION (%) (6)
	Type (2)	τ^a (3)			
E/S0	Exponential	1	2.5	4 ^b	28
Sab/Sbc	Exponential	4	1.0	4	47
Scd	Constant	...	0.2	4	13
Irr ^c	Constant	...	0.2	...	12

^a The e -folding time.

^b Values of $z_{\text{form}} = 4$ with $H_0 = 70 \text{ km s}^{-1} \text{ Mpc}^{-1}$, $\Omega_{\Lambda} = 0.7$ cosmology, corresponds to $z_{\text{form}} = 7$ in the Einstein–de Sitter universe.

^c Star-forming galaxies.

^d Age of 1 Gyr at every redshift.

this purpose, we have used the *ncmod* code from Gardner (1998), obtained from the author's Web site, to build galaxy number count predictions. The code follows the traditional approach of tracing back the evolution of the population of galaxies, assuming a $z = 0$ luminosity function (LF0) and galaxy-type mix, a redshift of formation z_f , and a star formation rate (SFR) history for each class of galaxies. The galaxy characteristics of the model are shown in Table 8. The models split the $z = 0$ population into three main types: ellipticals, spirals, and irregulars or star-forming galaxies. We use a characterization of galaxy properties (metallicity and SFR) similar to that of Gardner (1998; see Table 8). The redshift of formation used for all galaxy types is $z_{\text{form}} = 4$, corresponding to an age = 12 Gyr, for our adopted Λ -model ($H_0 = 70 \text{ km s}^{-1} \text{ Mpc}^{-1}$, $\Omega_{\Lambda} = 0.7$, $\Omega_M = 0.3$), and $z_{\text{form}} = 7$ for a flat, Einstein–de Sitter universe ($H_0 = 50$, $q_0 = 0.5$, age = 12.5 Gyr). The spectrophotometric population synthesis models of Bruzual & Charlot (1993, 1995 version), with Salpeter stellar initial mass function (IMF), are used to compute the evolution of the galaxy luminosities. The $z = 0$ Schechter (1976) parameterization of the luminosity function has been taken from Gardner et al. (1997; Cole et al. [2001] give the luminosity function transformation to the Λ -cosmology). For our cosmologies, the resulting parameters are given in Table 9. The local galaxy mix by Ellis (1983) has been used, but the late spirals are split into two groups: Sbc and irregular star-forming galaxies (col. [6] of Table 8). Other definitions of the galaxy mix, such as those by Tinsley (1980) or Pence (1976), hardly change the resulting count model up to $K = 21$ (the Tinsley mix predicts lower counts for $K > 21$). Figure 11a shows the number count prediction for the two cosmological models described above.

Number counts from these models are approximately featureless in the magnitude range of the data and clearly fail to reproduce the change of slope at $K_s = 17.5$. While a variety of parameters may modify the count predictions, prob-

TABLE 9
LUMINOSITY FUNCTIONS

Cosmology	M^*	α	ϕ^* (Mpc^{-3})
$H_0 = 70$, $\Omega_{\Lambda} = 0.7$, $\Omega_M = 0.3$	-24.07	-1.00	4.94×10^{-3}
$H_0 = 50$, $q_0 = 0.5$	-24.63	-0.91	1.99×10^{-3}

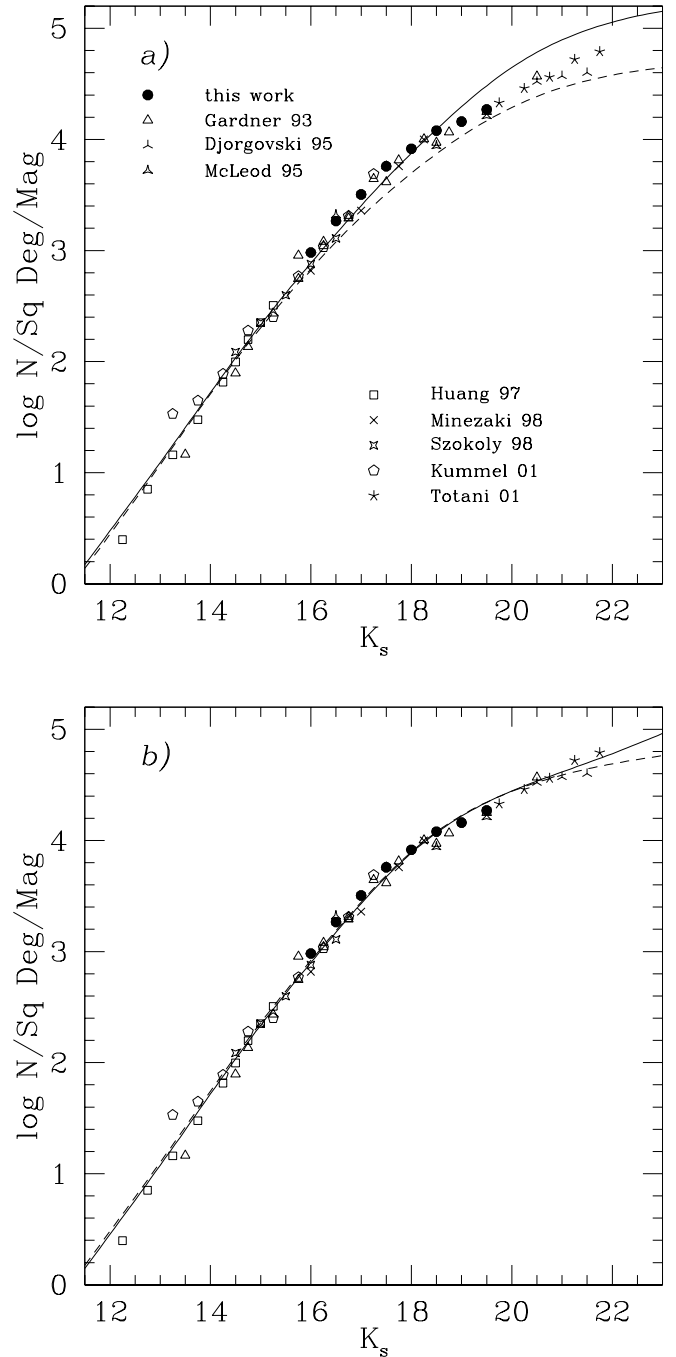


FIG. 11.—(a) Complete galaxy number counts in K_s from our and other surveys, compared with models. The dashed line corresponds to the Einstein–de Sitter model ($H_0 = 50 \text{ km s}^{-1} \text{ Mpc}^{-1}$, $q_0 = 0.5$), and the solid line corresponds to the Λ -model ($H_0 = 70 \text{ km s}^{-1} \text{ Mpc}^{-1}$, $\Omega_{\Lambda} = 0.7$, $\Omega_M = 0.3$). Symbols are as in Fig. 10. (b) The same as Λ -model as in (a), but galaxy formation is delayed down to $z = 2$ for ellipticals and early-type spirals and to $z = 1$ to late-type spirals (dashed line), and a population of dwarf star-forming galaxies is included (solid line).

ably the strongest assumption is the $z_{\text{form}} = 4$ common for all galaxy types. Delaying z_{form} for some or all of the types is the most natural way to improve the fit to the data by generating the change of slope in the counts at intermediate magnitudes. Delayed galaxy formation is also required to account for the bluing of intrinsic galaxy colors reported by Gardner et al. (1993). To approximately reproduce the change of slope of the number counts, we need to delay the

bulk of star formation to quite low values, $z_{\text{form}} \sim 2$ in the Λ -model (age = 10.2 Gyr) for most of both elliptical and spiral galaxies, and to introduce a star-forming dwarf galaxy population at all redshifts. To do so, we give the irregular galaxies a steep, faint slope of $\alpha = -1.5$, balanced by a fainter $M_K^* = -23.12$ and $\phi^* = 7.5 \times 10^{-3}$, the same as Gardner (1998). Figure 11b shows the fit of the data when star formation is delayed to $z = 2$ for ellipticals and early-type spiral galaxies and to $z = 1$ to late-type spirals, and a star-forming dwarf galaxy population is included at all redshifts.

8. SUMMARY

K_s -band galaxy number counts in two fields of the COSMOS survey, Coppi and Groth, have been presented. The combination of wide area (~ 180 arcmin²) and depth ($K_s = 21.0$) yields counts that cover the range $14.5 < K_s < 21.0$ with good statistics. The counts have been corrected for detection efficiency, measured separately for three different size bins, in each of the 14 camera pointings. Two half-exposure images of each pointing, made with complementary halves of the data, have been used to identify and remove spurious detections. Star-galaxy separation has been reliably performed using *HST* images in the Groth strip field and using the stellarity index from SExtractor together with color-color diagrams in the Coppi field.

Comparison to a compilation of shallow wide-area and deep pencil-beam surveys, covering the range from $K = 10$ to $K = 24$, shows a very good correspondence especially considering “complete data,” defined here as number count data where efficiency corrections are less than 5% and where there are more than 10 raw detected counts. Our data, as well as the complete data from other surveys, confirm the change in the slope at $K_s \sim 17.5$ reported in Gardner et al.

(1993). Our data yield slopes of ~ 0.54 in the range from $K_s = 15.5$ to $K_s = 17.5$ and ~ 0.25 from $K_s = 17.5$ to $K_s = 19.5$. The slopes are comparable to those of Gardner et al. (1993). The measured slope at the faint end puts limits to the contribution of faint, undetected galaxies to the extragalactic background light (EBL) in the K -band. Assuming no upturn in the number counts at magnitudes fainter than $K_s = 21.0$, we have calculated a limit to the total contribution to the EBL in the K -band from galaxies of $\nu I_\nu = 10.5$ nW m⁻² sr⁻¹; or $\sim 50\%$ of the measured EBL.

The shape of the number count distribution cannot be fitted with galaxy formation schemes that place galaxy formation at $z_{\text{form}} \geq 4$ in a Λ -dominated universe ($H_0 = 70$ km s⁻¹ Mpc⁻¹, $\Omega_\Lambda = 0.7$, $\Omega_M = 0.3$) or $z_{\text{form}} \geq 7$ in an Einstein-de Sitter universe. Reproducing the change in the number count slope at $K \sim 17.5$ requires both a delay in the galaxy formation epoch to quite low values, $z_{\text{form}} \leq 2$ for elliptical and spiral galaxies, and the presence of a population of star-forming dwarfs at all redshifts (Λ -dominated universe).

We thank the referee, Jonathan Gardner, for his comments, which helped improve the manuscript. We acknowledge useful discussions on number counts with Matthew Bershadsky, David Koo, and James Lowenthal. James Lowenthal, Peter Hammersley, and José Acosta-Pulido gave us invaluable help and insights on NIR image reduction. This research has made use of the *HST* archive and the MDS online database. The Medium Deep Survey catalog is based on observations with the NASA/ESA *Hubble Space Telescope*, obtained at the Space Telescope Science Institute, which is operated by AURA, Inc., under NASA contract NAS 5-26555. The MDS analysis was funded by the *HST* WFPC2 Team and STScI grants GO2684, GO6951, GO7536, and GO8384 to Richard Griffiths and Kavan Ratnatunga at Carnegie Mellon University.

APPENDIX

ERROR ESTIMATION

The error estimation was done independently for each object class in each pointing. This is necessary since we take into account the errors in detection efficiency determination (see § 5). In each magnitude bin two sources of error are considered: counting errors that are parameterized with the approximate relations (see Gehrels 1986)

$$\sigma_u^N = \sqrt{n + \frac{3}{4}} + 1, \quad \sigma_l^N = n - n \left(1 - \frac{1}{9n} - \frac{1}{3\sqrt{n}} \right)^3 \quad (\text{A1})$$

and errors in the determination of detection efficiency df . The counts are calculated in each pointing in $\frac{1}{2}$ magnitude bins and are given in units of $N \text{ mag}^{-1} \text{ deg}^{-2}$ using

$$A_{ij} = \frac{2N_{ij}}{a_j df_{ij}}, \quad (\text{A2})$$

where i is each of the three object classes, j corresponds to each of the 14 pointings, and a_j is the covered area. Error propagation for 1σ error gives

$$\sigma^{A_{ij}} = \frac{2}{a_j} \sqrt{\left(\frac{\sigma_u^{N_{ij}}}{df_{ij}} \right)^2 + \left(\sigma^{df_{ij}} \frac{N_{ij}}{df_{ij}^2} \right)^2}. \quad (\text{A3})$$

The same formula is used to obtain the 1σ confidence upper and lower limits,

$$\sigma_l^{A_{ij}} = \frac{2}{a_j} \sqrt{\left(\frac{\sigma_l^{N_{ij}}}{df_{ij}} \right)^2 + \left(\sigma^{df_{ij}} \frac{N_{ij}}{df_{ij}^2} \right)^2}, \quad \sigma_u^{A_{ij}} = \frac{2}{a_j} \sqrt{\left(\frac{\sigma_u^{N_{ij}}}{df_{ij}} \right)^2 + \left(\sigma^{df_{ij}} \frac{N_{ij}}{df_{ij}^2} \right)^2}. \quad (\text{A4})$$

The counts in each pointing are the sum of the corrected counts of each object class, so the errors are

$$\sigma_l^{A_j} = \sqrt{\sum_i \left(\sigma_l^{A_{ij}}\right)^2 + \left(\sigma_l^{A_{*j}}\right)^2}, \quad \sigma_u^{A_j} = \sqrt{\sum_i \left(\sigma_u^{A_{ij}}\right)^2 + \left(\sigma_u^{A_{*j}}\right)^2}, \quad (\text{A5})$$

where the terms $\sigma_{l,u}^{A_{*j}}$ are considered only in Groth pointings in which the number of stars is subtracted from the number of objects.

Finally, the counts of different pointings A_j are combined with the weighted mean,

$$\sum_j (a_j) A = \sum_j (a_j A_j); \quad (\text{A6})$$

then

$$\sigma_l^A = \frac{1}{\sum_j (a_j)} \sqrt{\sum_j \left(a_j \sigma_l^{A_j}\right)^2}, \quad \sigma_u^A = \frac{1}{\sum_j (a_j)} \sqrt{\sum_j \left(a_j \sigma_u^{A_j}\right)^2}. \quad (\text{A7})$$

REFERENCES

- Aguerri, J. A. L., & Trujillo, I. 2002, *MNRAS*, 333, 633
 Babul, A., & Rees, M. J. 1992, *MNRAS*, 255, 346
 Balcells, M. 1998, *Ap&SS*, 263, 361
 Bershad, M. A., Lowenthal, J. D., & Koo, D. C. 1998, *ApJ*, 505, 50
 Bertin, E., & Arnouts, S. 1996, *A&AS*, 117, 393
 Bruzual, G. A., & Charlot, S. 1993, *ApJ*, 405, 538
 Cole, S., et al. 2001, *MNRAS*, 326, 255
 Coppi, P. S., & Guzmán, R. 2001, Two Years of Science with *Chandra*, Abstracts from the Symposium held in Washington, DC, 2001 September 5–7
 Cowie, L. L., Gardner, J. P., Hu, E. M., Songaila, A., Hodapp, L. W., & Wainscoat, R. J. 1994, *ApJ*, 434, 114
 Coppi, P. S., Guzmán, R., Zepf, S., Roscherr, B., & Woo, J. H. 2000, *AAS/HEAD Meeting*, 32, 2619
 Djorgovski, S. G., et al. 1995, *ApJ*, 438, L13
 Ellis, R. S. 1983, in *The Origin and Evolution of Galaxies*, ed. B. J. T. Jones & J. E. Jones (Dordrecht: Reidel), 255
 Elston, R. 1998, *Proc. SPIE*, 3354, 404
 Gardner, J. P. 1998, *PASP*, 110, 291
 Gardner, J. P., Cowie, L. L., & Wainscoat, R. J. 1993, *ApJ*, 415, L9
 Gardner, J. P., Sharples, R. M., Carrasco, B. E., & Frenk, C. S. 1996, *MNRAS*, 282, L1
 Gardner, J. P., Sharples, R. M., Frenk, C. S., & Carrasco, B. E. 1997, *ApJ*, 480, L99
 Gehrels, N. 1986, *ApJ*, 303, 336
 Glazebrook, K., Peacock, J. A., Collins, C. A., & Miller, L. 1994, *MNRAS*, 266, 65
 Gorjian, V., Wright, E. L., & Chary, R. R. 2000, *ApJ*, 536, 550
 Groth, E. J., Kristian, J. A., Lynds, R., O’Neil, E. J., Balsano, R., Rhodes, J., & Idt, W. 1994, *BAAS*, 185, 5309
 Guzmán, R., Gallego, J., Koo, D. C., Phillips, A. C., Lowenthal, J. D., Faber, S. M., Illingworth, G. D., & Vogt, N. P. 1997, *ApJ*, 489, 559
 Guzmán, R., Jangren, A., Koo, D. C., Bershad, M. A., & Simard, L. 1998, *ApJ*, 495, L13
 Hauser, M. G., & Dwek, E. 2001, *ARA&A*, 39, 249
 Huang, J.-S., Cowie, L. L., Gardner, J. P., Hu, E. M., Songaila, A., & Wainscoat, R. J. 1997, *ApJ*, 476, 12
 Huang, J.-S., et al. 2001, *A&A*, 368, 787
 ———. 2001, *A&A*, 370, 384
 Lilly, S. J., Cowie, L. L., & Gardner, J. P. 1991, *ApJ*, 369, 79
 Lowenthal, J. D., et al. 1997, *ApJ*, 481, 673
 Maddox, S. J., Sutherland, W. J., Efstathiou, G., Loveday, J., & Peterson, B. A. 1990, *MNRAS*, 247, 1
 Manescau, A., et al. 2002, *Proc. SPIE*, 4411, 39
 Marleau, F. R., & Simard, L. 1998, *ApJ*, 507, 585
 Martini, P. 2001, *AJ*, 121, 598
 McCracken, H. J., Metcalfe, N., Shanks, T., Campos, A., Gardner, J. P., & Fong, R. 2000, *MNRAS*, 311, 707
 McLeod, B. A., Bernstein, G. M., Rieke, M. J., Tollestrup, E. V., & Fazio, G. G. 1995, *ApJS*, 96, 117
 Metcalfe, N., Shanks, T., Fong, R., & Jones, L. R. 1991, *MNRAS*, 249, 498
 Minezaki, T., Kobayashi, Y., Yoshii, Y., & Peterson, B. A. 1998, *ApJ*, 494, 111
 Moustakas, L. A., Davis, M., Graham, J. R., Silk, J., Peterson, B. A., & Yoshii, Y. 1997, *ApJ*, 475, 445
 Pence, W. 1976, *ApJ*, 203, 39
 Persson, S. E., Murphy, D. C., Krzeminski, W., Roth, M., & Rieke, M. J. 1998, *AJ*, 116, 2475
 Phillips, A. C., Guzmán, R., Gallego, J., Koo, D. C., Lowenthal, J. D., Vogt, N. P., Faber, S. M., & Illingworth, G. D. 1997, *ApJ*, 489, 543
 Ratnatunga, K. U., Griffiths, R. E., & Ostrander, E. J. 1999, *AJ*, 118, 86
 Ratnatunga, K. U., Ostrander, E. J., Griffiths, R. E., & Im, M. 1995, *ApJ*, 453, L5
 Roche, N., Ratnatunga, K. U., Griffiths, R. E., Im, M., & Neuschaefer, L. 1996, *MNRAS*, 282, 1247
 Saracco, P., D’Odorico, S., Moorwood, A., Buzzoni, A., Cuby, J.-G., & Lidman, C. 1999, *A&A*, 349, 751
 Saracco, P., Iovino, A., Garilli, B., Maccagni, D., & Chincarini, G. 1997, *AJ*, 114, 887
 Schechter, P. 1976, *ApJ*, 203, 297
 Spagna, A. 2001 *Guide Star Requirements for NGST: Deep NIR Star Counts and Guide Star Catalog (STScI-NGST-R-0013B; Baltimore: STScI)*
 Stanford, S. A., Eisenhardt, P. R., & Dickinson, M. E. 1995, *ApJ*, 450, 512
 Steidel, C. C., Adelberger, K. L., Giavalisco, M., Dickinson, M., & Pettini, M. 1999, *ApJ*, 519, 1
 Steidel, C. C., Giavalisco, M., Pettini, M., Dickinson, M., & Adelberger, K. L. 1996, *ApJ*, 462, L17
 Tinsley, B. M. 1980, *ApJ*, 241, 41
 Totani, T., Yoshii, Y., Iwamuro, F., Maihara, T., & Motohara, K. 2001, *ApJ*, 550, L137
 Totani, T., Yoshii, Y., Maihara, T., Iwamuro, F., & Motohara, K. 2001, *ApJ*, 559, 592
 Tyson, J. A. 1988, *AJ*, 96, 1
 Väisänen, P., Tollestrup, E. V., Willner, S. P., & Cohen, M. 2000, *ApJ*, 540, 593
 Wright, E. L. 2001, *ApJ*, 553, 538